3D Rotation Estimation from Catadioptric Lines without Correspondences using the Radon Transform, Harmonic Analysis and Conformal Geometric Algebra

C. López-Franco, L. Falcón-Morales, N. Arana-Daniel and E. Bayro-Corrochano

Abstract— **Omnidirectional vision systems provide a large field of view, this property can benefit algorithms developed to solve robotic tasks. One interesting problem is the estimation of the rotation between omnidirectional images. Since the images taken by omnidirectional sensors can be mapped to a sphere, the problem of attitude estimation of a 3D camera rotation can be treated as a problem of estimating rotations between spherical images. Usually, this rotation estimation problem has been solved using point correspondences or gradient information of the points of the images. The respective computational time is very time consuming for these point algorithms. In this paper we present an effective solution to the attitude estimation problem with the radon transform, which uses line information instead of points. The algorithm is defined under the conformal geometric algebra framework, to take advantage of the geometric information provided by the omnidirectional projection.**

I. INTRODUCTION

In this paper we apply the classic theory of Harmonic Analysis to recover information given by the lines of the omnidirectional images of a catadioptric system, which consists of a conventional camera and a convex mirror. In order to be able to model the catadioptric sensor geometrically, it must satisfy the restriction that all the measurements of light intensity pass through only one point in the space (effective viewpoint). The complete class of mirrors that satisfy such restriction where analyzed by Baker and Nayar [1]. In [2] the authors deal with the epipolar geometry of two catadioptric sensors. Later, in [3] a general model for central catadioptric image formation was given. Also, a representation of this general model using the conformal geometric algebra was shown in [4]. In this work we use the model proposed in [5] to compute analytically the projection and back projection of $3D$ lines. Using the spherical equivalence, we propose an image analysis using the Fourier transform on the unit sphere S^2 and on the rotation group $\mathcal{SO}(3)$. In recent years harmonic analysis has been used in computer vision to obtain $3D$ rotations with the Radon and Hough transforms. Harmonic analysis is used in [6] to obtain the *essential matrix* of two omnidirectional images and in [7] to recover the relative orientation of two cameras using the Radon transform as a *correlation of points* on S^2 and $\mathcal{SO}(3)$ without correspondences.

II. GEOMETRIC ALGEBRA

In general the geometric algebra $\mathcal{G}_n = \mathcal{G}(\mathcal{V}^n)$ is constructed over a vector space $\mathcal{V}^n$ in which the geometric product is defined. We also denote with $\mathcal{G}_{p,q,r}$ a geometric algebra over $\mathcal{V}^{p,q,r}$ where p, q, r denote the signature p, q, r of the algebra. The geometric product of two bases vectors e_i, e_j is defined as

$$
e_i e_j = \begin{cases} 1 & \text{for } i = j \in 1, ..., p \\ -1 & \text{for } i = j \in p+1, ..., p+q \\ 0 & \text{for } i = j \in p+q+1, ..., p+q+r \\ e_i \wedge e_j & \text{for } i \neq j \end{cases}
$$

$$(1)$$

A generic element in $\mathcal{G}_n$ is called a *multivector*. Every multivector M can be written in the expanded form

$$
M = \sum_{i=0}^{n} \langle M \rangle_i \tag{2}
$$

where $\langle M \rangle_i$ represents the i-vector part.

An important operation that is used in the geometric algebra is called reversion denoted by "˜" and defined by

$$
\widetilde{\langle M \rangle}_i = (-1)^{\frac{i(i-1)}{2}} \left\langle \widetilde{M_i} \right\rangle, \text{ for } M \in \mathcal{G}_n, \ 0 \leq i \leq n. \tag{3}
$$

In geometric algebra the highest grade blade is called *pseudoscalar*. The *unit pseudoscalar* is defined as $I = e_1 \wedge e_2 \wedge \cdots \wedge e_n$ and is denoted with with $I_{p,q}$. The unit pseudoscalar can be used to define the dual of a multivector M in $\mathcal{G}_n$ as

$$
M^* = M I_n^{-1} , \tag{4}
$$

where $I_n I_n^{-1} = 1$ and I_n^{-1} differs from I_n by at most a sign . The dual of an r-blade is an (n-r)-blade, in particular the dual of the pseudoscalar is a scalar. For more details, the interested reader is referred to [8] and [9].

A. Conformal Geometric Algebra

The conformal geometric algebra (CGA) embeds the vector space $\mathcal{V}^n$ in a higher dimensional space $\mathcal{G}_{n+1,1} = \mathcal{G}(\mathcal{V}^{n+1,1})$, called the homogeneous conformal space [10]. In the (CGA) we add two extra bases to our Euclidean vector space; these are e_+ and e_-, where $e_+^2 = 1$ and $e_-^2 = -1$. With this two bases we define two null vectors $e_0 = \frac{e_- - e_+}{2}$ and $e_\infty = e_- + e_+$. Where e_0 is interpreted as the origin of the coordinate system and e_∞ is interpreted as the point at infinity. The outer product of the bases e_+ and e_- defines the bivector $E = e_+ \wedge e_-$, which represents the Minkowski plane.

A point in the conformal space is defined as

$$X = \mathbf{x} + \frac{1}{2}\mathbf{x}^2 e_\infty + e_0 . \tag{5}$$

The circle C^* is defined with the outer product of three points lying on it, $C^* = A \wedge B \wedge C$. If one of the points is the point at infinity then we get the line

$$L^* = A \wedge B \wedge e_\infty = dE + m e_\infty \tag{6}$$

where $d = (b - a)$ and $m = (a \wedge b)I_3$, representing the direction and moment of the line L^* respectively. The direction can be extracted from the line L^* as

$$d = -(L^* \cdot E) \tag{7}$$

B. Rigid Motion

In $\mathcal{G}_n$ the rotation transformations can be applied to objects using a *rotor*. Let $\mathcal{R}$ denote the rotation operation

$$\mathcal{R}(X) = RX\widetilde{R}, \tag{8}$$

where x is any multivector.

The translation of entities is carried out with a translator $T = \left(1 + \frac{e_\infty \mathbf{t}}{2}\right)$, where $\mathbf{t}$ represents the translation vector. The translator is applied in the same way as the rotator and also to any entity of the CGA.

III. PARACATADIOPTRIC IMAGE FORMATION AND CONFORMAL GEOMETRIC ALGEBRA

In [5] the authors shown the equivalence of the paracatadioptric projection and the projection on two spheres S and S_0.

A. Paracatadioptric point projection

Let X be a point in the space, its projection onto the sphere can be found by finding the line passing through it and the sphere center, that is

$$L^* = S \wedge X \wedge \mathbf{e}_\infty . \tag{9}$$

Then, this line is intersected with the sphere S

$$Q = S \cdot L^* , \tag{10}$$

where Q denotes a *point-pair* ($Q^* = X_1 \wedge X_2$). The point closest to X can be found with

$$X_s = \frac{Q^* - |Q^*|}{Q^* \cdot \mathbf{e}_\infty} . \tag{11}$$

Finally, the projection onto the paracatadioptric image plane is simply

$$X_c = S_0 X_s \widetilde{S_0} . \tag{12}$$

The point X_c is the projection of the point X onto the catadioptric image plane, which is exactly the same point obtained through the parabolic projection.

B. Back Projection of Point Images

Given a point X_c on the catadioptric image, its projection to the sphere is simply $X_s = \widetilde{S_0}X_c S_0$. The point X_s lies on a line that passes through the sphere center, that is $L^* = P_1 \wedge S \wedge \mathbf{e}_\infty$. The original point X, also, lies on this line, but since we have a single image the depth can not be determined and thus the point X can no be calculated.

C. Paracatadioptric Line Projection

Given a line L in 3D space its projection onto the paracatadioptric image plane is in general a circle, but when the line is parallel to the optical axis of the mirror its projection is a line. The paracatadioptric projection of the line can be found by defining a plane containing the line and passing through the center of the sphere S

$$\Pi^* = L^* \wedge S . \tag{13}$$

Then, the plane Π^* is intersected with the sphere to obtain a great circle defined as

$$C_s^* = S \cdot \Pi^* . \tag{14}$$

Finally, the circle C_s is projected onto the image plane using

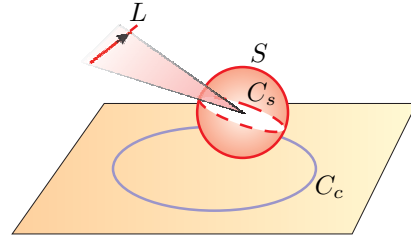$$C_c^* = S_0 C_s^* \widetilde{S_0} . \tag{15}$$

Fig. 1. Projection of the line L onto the paracatadioptric image plane.

D. Back-projection of Paracatadioptric Lines

Let C_c^* be a paracatadioptric projection of a line in 3D space, its projection onto the sphere S can be found simply with

$$C_s^* = \widetilde{S_0} C_c^* S_0 . \tag{16}$$

The plane where the circle lies on is defined as

$$\Pi_s^* = C_s^* \wedge e_\infty . \tag{17}$$

The paracatadioptric projection of a line L^* in 3D space (Fig. 1) can be found by defining a plane where the line L^* and the center of the sphere S lie, that is $\Pi^* = L^* \wedge S$.

E. Radon transform with lines

The Radon transform was written as a correlation of points between two omnidirectional images in [11], to obtain the Euler angles of the relative orientation between the two cameras. This Radon transform with points is defined as

$$G(R, t) = \int_{p \in S^2} \int_{q \in S^2} g(p, q) \Delta(Rp, q, t) dp dq, \qquad (18)$$

where the *similarity* function g is a measure of how likely the SIFT points p and q are the projections of the same scene point and the Δ function is the Kronecker delta function relating the points p and q with the epipolar constraint of a stereo camera system. For sake of simplicity we are calling *SIFT points* to the SIFT descriptors returned by the SIFT algorithm [12].

To extend the Radon transform as a correlation in the space of lines to estimate pure rotations, we need to redefine the integral (18), the similarity and the delta functions to the space of lines.

Let L and L' represent two lines in the 3D space, defined in the CGA, related with a rotation $L' = RL\widetilde{R}$ or $L = \widetilde{R}L'R$. The direction of the lines δ and δ' can be extracted from the lines using (7). Let Π and Π' represent respectively two planes defined by the lines L and L' and the center of the sphere S, which can be computed with (13). The normal vector of the plane Π can be computed with

$$\eta = -(\Pi^* I \wedge E) E. \qquad (19)$$

Since η and $\widetilde{R}\delta'R$ are orthogonal, we have that $\eta \cdot (\widetilde{R}\delta'R) = 0$. This constraint will be used to define the delta function and the integral. Thus, the integral of the *Radon transform on lines* is

$$G(R) = \int_{\delta' \in S^2} \int_{\eta \in S^2} g(\eta, \delta') \Delta(\eta \cdot (\widetilde{R}\delta'R)) d\eta d\delta' \qquad (20)$$

where g is a *similarity function* between the lines of both images and Δ the delta Kronecker function on the constraint of lines. So, (20) can be used as a correlation function between g and Δ, where $g, \Delta : S^2 \times S^2 \to \{0, 1\}$.

Applying the spherical Fourier expansion to the similarity function g of (20), we have

$$g(\omega_1, \omega_2) =$$
$$\sum_{l_1=0}^{bw-1} \sum_{|m_1| \leq l_1} \sum_{l_2=0}^{bw-1} \sum_{|m_2| \leq l_2} \hat{g}_{m_1 m_2}^{l_1 l_2} Y_{l_1}^{m_1}(\omega_1) Y_{l_2}^{m_2}(\omega_2), \quad (21)$$

where Y_l^m are the spherical harmonics

$$Y_l^m(\theta, \phi) = \sqrt{\frac{(2l+1)(l-m)!}{4\pi(l+m)!}} P_l^m(\cos\theta) e^{im\phi}. \qquad (22)$$

In (21) we used $g(\omega_1, \omega_2)$ instead of $g(\eta, \delta')$ to simplify notation.

Similarly, we get the expansion of the Δ function for each $(\omega_1, \omega_2) \in S^2 \times S^2$ and $R \in \mathcal{SO}(3)$ as

$$\Delta(\omega_1, R\omega_2\widetilde{R}) =$$
$$\sum_{p_1=0}^{bw-1} \sum_{|k_1| \leq p_1} \sum_{p_2=0}^{bw-1} \sum_{|k_2| \leq p_2} \hat{\Delta}_{k_1 k_2}^{p_1 p_2}(R) Y_{p_1}^{k_1}(\omega_1) Y_{p_2}^{k_2}(\omega_2). \quad (23)$$

Since $\omega_1 \cdot (R\omega_2\widetilde{R}) = \omega_2 \cdot (\widetilde{R}\omega_1 R) = 0$, we can write

$$\hat{\Delta}_{k_1 k_2}^{p_1 p_2}(\omega_1, \widetilde{R}\omega_2 R) \qquad (24)$$

instead of $\hat{\Delta}_{k_1 k_2}^{p_1 p_2}(R)$ in (23) and by the *shift theorem* we have

$$\hat{\Delta}_{k_1 k_2}^{p_1 p_2}(\omega_1, \widetilde{R}\omega_2 R) = \sum_{|b| \leq p_2} U_{bk_2}^{p_2}(R) \hat{\Delta}_{k_1 b}^{p_1 p_2}, \qquad (25)$$

where $\hat{\Delta}_{k_1 b}^{p_1 p_2} \equiv \hat{\Delta}_{k_1 b}^{p_1 p_2}(\omega_1, \omega_2)$. Substituting (21), (23) and (25) in (20) we get

$$G(R) = \int_{\omega_1 \in S^2} \int_{\omega_2 \in S^2}$$
$$\left[\sum_{l_1} \sum_{|m_1| \leq l_1} \sum_{l_2} \sum_{|m_2| \leq l_2} \hat{g}_{m_1 m_2}^{l_1 l_2} Y_{l_1}^{m_1}(\omega_1) Y_{l_2}^{m_2}(\omega_2) \right] \cdot$$
$$\cdot \left[\sum_{p_1} \sum_{|k_1| \leq p_1} \sum_{p_2} \sum_{|k_2| \leq p_2} \cdot \left\{ \sum_{|b| \leq p_2} \overline{U_{bk_2}^{p_2}(R) \hat{\Delta}_{k_1 b}^{p_1 p_2}} \right\} \cdot \right.$$
$$\left. \cdot \overline{Y_{p_1}^{k_1}(\omega_1) Y_{p_2}^{k_2}(\omega_2)} \right] d\omega_1 d\omega_2. \quad (26)$$

Because the spherical harmonics are an orthonormal set

$$\int_{\omega \in S^2} Y_l^m(\omega) \overline{Y_{l'}^{m'}(\omega)} d\omega = \delta_{ll'} \delta_{mm'}, \qquad (27)$$

which can be applied in (26) to obtain

$$G(R) =$$
$$\sum_{l_1} \sum_{|m_1| \leq l_1} \sum_{l_2} \sum_{|m_2| \leq l_2} \sum_{p_1} \sum_{|k_1| \leq p_1} \sum_{p_2} \sum_{|k_2| \leq p_2}$$
$$\left\{ \sum_{|b| \leq p_2} \hat{g}_{m_1 m_2}^{l_1 l_2} \overline{\hat{\Delta}_{k_1 b}^{p_1 p_2}} \overline{U_{bk_2}^{p_2}(R)} \right\} \cdot$$
$$\cdot \left\{ \int_{\omega_1 \in S^2} \underbrace{Y_{l_1}^{m_1}(\omega_1) \overline{Y_{p_1}^{k_1}(\omega_1)}}_{\delta_{l_1 p_1} \delta_{m_1 k_1}} d\omega_1 \cdot \right.$$
$$\left. \cdot \int_{\omega_2 \in S^2} \underbrace{Y_{l_2}^{m_2}(\omega_2) \overline{Y_{p_2}^{k_2}(\omega_2)}}_{\delta_{l_2 p_2} \delta_{m_2 k_2}} d\omega_2 \right\} \qquad (28)$$
$$= \sum_{l_1} \sum_{|m_1| \leq l_1} \sum_{l_2} \sum_{|m_2| \leq l_2} \sum_{|b| \leq p_2}$$
$$\hat{g}_{m_1 m_2}^{l_1 l_2} \overline{\hat{\Delta}_{m_1 b}^{l_1 l_2}} U_{bm_2}^{l_2}(R). \qquad (29)$$

Let us remember that in $\mathcal{SO}(3)$ the elements U's are orthonormal,

$$\int_{R \in \mathcal{SO}(3)} U_{mk}^l(R) U_{m'k'}^{l'}(R) dR = \delta_{ll'} \delta_{mm'} \delta_{kk'}. \quad (30)$$

Now, for each $l_2' = 0, 1, \ldots, (bw - 1)$ and $b', m_2' \in \{-l_2, \ldots, -1, 0, 1, \ldots, l_2\}$ let us multiply by $U_{b'm_2'}^{l_2'}(R)$ in both sides of (28), taking the integration on $\mathcal{SO}(3)$ and using (30) to obtain

$$\int_{\mathcal{SO}(3)} G(R) U_{b'm_2'}^{l_2'} dR =$$

$$\sum_{l_1} \sum_{|m_1| \leq l_1} \sum_{l_2} \sum_{|m_2| \leq l_2} \sum_{|b| \leq p_2} \cdot$$

$$\cdot \hat{g}_{m_1 m_2}^{l_1 l_2} \overline{\hat{\Delta}_{m_1 b}^{l_1 l_2}} \underbrace{\int_{\mathcal{SO}(3)} U_{b'm_2'}^{l_2'}(R) \overline{U_{bm_2}^{l_2}(R)} dR}_{\delta_{l_2 l_2'} \delta_{bb'} \delta_{m_2 m_2'}} \quad (31)$$

$$= \sum_{l_1} \sum_{|m_1| \leq l_1} \hat{g}_{m_1 m_2'}^{l_1 l_2'} \overline{\hat{\Delta}_{m_1 b'}^{l_1 l_2'}}. \quad (32)$$

From the last equality we have the $3D$ Fourier transform $\hat{G}$ of G on $\mathcal{SO}(3)$. Indeed, rewriting the indexes as $l_2' \to l_2$, $b' \to b$ and $m_2' \to m_2$, the Fourier transform $\hat{G}$ of G on the rotation group $\mathcal{SO}(3)$ is given as

$$\hat{G} = (\hat{G}_{bm_2}^{l_2}) \quad (33)$$

where $l_2 = 0, 1, \ldots, (bw - 1)$ and $b, m_2 \in \{-l_2, \ldots, -1, 0, 1, \ldots, l_2\}$ and the entries are

$$\hat{G}_{bm_2}^{l_2} = \sum_{l_1} \sum_{|m_1| \leq l_1} \hat{g}_{m_1 m_2}^{l_1 l_2} \overline{\hat{\Delta}_{m_1 b}^{l_1 l_2}}. \quad (34)$$

Our expression (34) obtained for lines and pure rotations is consistent with the formula for points obtained in [7] for the case of a pure rotation.

Although we know how to calculate the analytical expressions of the continuous Fourier and Radon transforms in spherical coordinates, it is necessary to use a discretization process for their applications with real omnidirectional images. Given a function on the space $L^2(S^2)$ with bandlimit bw, its spherical Fourier transform SFT can be obtained with the FFT algorithm of order $\mathcal{O}(bw^2 \log^2 bw)$ on S^2, see Driscoll and Healy [13], for details. Similarly, we can use the FFT algorithm of order $\mathcal{O}(bw^3 \log^2 bw)$ in the case of the rotation space $\mathcal{SO}(3)$, see Kostelec and Rockmore [14], for details.

IV. Similarity, Characteristic and Cost Functions

Now that we have the analytical expression of the Radon transform with lines (20), let us see how to use it during the discretized process.

Suppose that the omnidirectional camera has performed a pure $3D$ rotation. Using the model [5] we compute the back-projection of lines projected onto the paracatadioptric
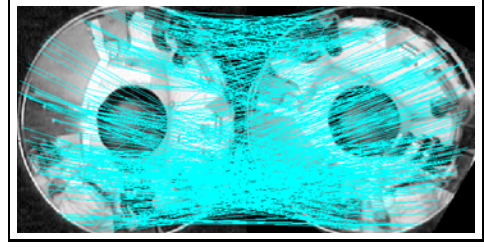

Fig. 2. This image is the output of the SIFT algorithm to obtain a reduction of the searching space. This is not a perfect correspondence between the points of the two images, but can help us to reduce the searching space of points.

image plane. Let C_c^* denote the projection of a $3D$ line onto the paracatadioptric image plane, its back-projection C_s^* can be computed using (16). The plane Π passing through this plane is (17) and finally the normal vector of the plane can be computed with (19).

Given two omnidirectional images let us apply the SIFT algorithm [12] to obtain the SIFT points associated with them. See Figure 2. Now, choose randomly a set of these SIFT points. At the center of each of these points a mask of size $m \times m$ is applied. Now, for each set of SIFT points inside of each mask, we are going to find the *best fitting* circle using RANSAC and then use Levenberg-Marquardt with the following cost function to minimize

$$\min_{h,k,r} error = (x - h)^2 + (y - k)^2 - r^2 +$$

$$+ \left| \arctan\left(\frac{c_y - k}{c_x - h}\right) - \theta_c \right|. \quad (35)$$

The first terms are the constraint to get a circle of radius r centered on (h, k). The last term is the constraint verifying that the line passing through the center of the mask (c_x, c_y) and slope $tan(\theta)$, could be lined up to the average SIFT-vector with slope $tan(\theta_c)$ and initial point (c_x, c_y). See Figure 3. θ_c is the average angle of the SIFT-points inside the mask. Furthermore, we are considering only those SIFT-points inside the mask with SIFT-angles values θ in the interval $[\theta_c - \Delta\theta, \theta_c + \Delta\theta]$, for some $\Delta\theta > 0$. In this way we are considering the main tendency of the SIFT vectors inside the mask.

Let η be the point on S^2 associated to a circle of the first omnidirectional image plane. Taking the SIFT points on the second omnidirectional image and the mask of size $m \times m$ we can find, in the same way, the best fitting circle η' associated to η. Notice that even though we obtained one point to represent a circle, we still have the robustness of the process because this point is the normal vector of a fitting circle. Then the characteristic function Δ must obey the constraint for lines

$$\Delta(R\eta\widetilde{R}, \eta') = \delta(((R\eta\widetilde{R}) \wedge \eta') I_3^{-1}) \quad (36)$$

$$= \begin{cases} 1 & \text{if} \quad |(\mathcal{R}(\eta) \wedge \eta') I_3^{-1}| < \epsilon \\ 0 & \text{other case} \end{cases}$$
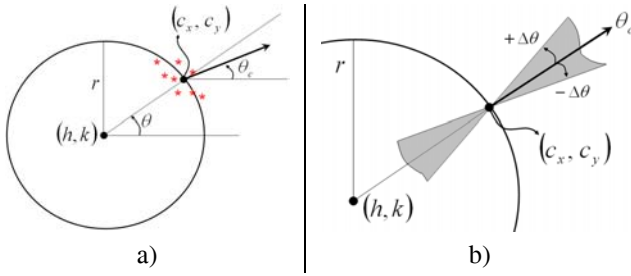
Fig. 3. (a) θ_c is the average angle of the angles of the SIFT vectors inside the mask $m \times m$. The arctan summand of the cost function (35) will try to line up the average SIFT vector with angle θ_c with respect to the line passing through the points (h, k) and (c_x, c_y). (b) Searching interval of the SIFT vectors.
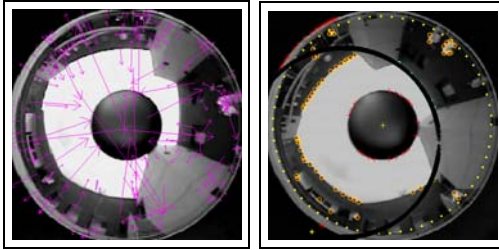

Fig. 4. (a) Vectors from the SIFT points. (b) One of the detected circles on a real image.

for $0 < \epsilon = \pi/(8 \; bw)$, where bw is the bandlimit of the discretization process. Thus, the Δ function (36) is measuring how close are the two circles η and η'. Finally, following the work in [7], we take the similarity function as

$$g(\tilde{\delta}, \tilde{\delta}') = exp\left\{-\left\|\tilde{\delta} - \tilde{\delta}'\right\|\right\} \qquad (37)$$

if $exp\left\{-\left\|\tilde{\delta} - \tilde{\delta}'\right\|\right\} > \epsilon'$ and zero in other case, and where $\|\cdot\|$ is the Euclidean norm and $\tilde{\delta}$ and $\tilde{\delta}'$ are the 128-dimensional SIFT vectors of the center points of each mask. $\epsilon' > 0$ is an arbitrary threshold.

In summary, the steps of the algorithm to recover the rotation only are:

Input: Two omnidirectional images.

Output: The 3D orientation relative between cameras.

1) Apply the SIFT algorithm to detect SIFT features.
2) Using the SIFT points detected on each image, we obtain the best fitting circles on each image.
3) Project each circle detected on the image plane onto the sphere using (16), compute their respective planes with (17) and compute their normal (19).
4) Apply equations (36) and (37) to obtain the functions Δ and g on $S^2 \times S^2$.
5) Compute the spherical Fourier transform of f and g, on $S^2 \times S^2$, that is, $\hat{f}$ and $\hat{g}$.
6) Using expression (34) compute $\hat{G}$, the Fourier transform of G on the rotation group $\mathcal{SO}(3)$.
7) Compute G from the inverse Fourier transform of $\hat{G}$.
8) Locate the maximum of $G(R)$ on $R = R(\alpha, \beta, \gamma)$ to obtain the orientation relative between cameras R.
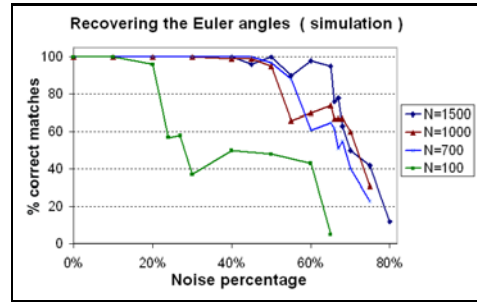

Fig. 5. Percentage of the correct matches of the algorithm versus percentage of noise for a bandlimit $B = 16$, generating N simulated correspondences lines.
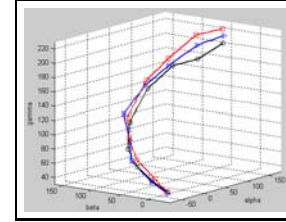

Fig. 6. Estimation of the Euler angles where the rotation axis is not parallel to the axis of the mirror. Square lines, triangle lines and circle lines are the result of the Radon with lines, Radon with points and exact values, respectively.

V. EXPERIMENTS

In this section we apply the Radon Transform using Lines to estimate rotations using real and synthetic images.

A. Noisy synthetic images

N 3D-lines were randomly generated and rotated with different Euler angles α, β, γ for perfect correspondence of the similarity and characteristic functions. Noisy lines were included on each image, that is, lines without correspondence on the other image.

N correspondences lines pairs in a range of 100 to 3000 were generated and then we recovered their Euler angles with different values of noise percentage. During the simulation process we had used the correspondence information only to measure the percentage of the correct matches of our algorithm, but obviously this information is not used with the real images. We can see from Figure 5 that even with a 60% of noise the algorithm was successful 80% of time, where in this particular case $N = 1500$.

Figure 6 depicts another simulation with bandlimit $bw = 32$. The mirror is rotated with a rotation axis not parallel to the axis mirror. Approximately every $25°$ the Euler angles were calculated with our Radon transform with lines. For an angle less than $180°$ the errors are in the same range of magnitude as the Radon transform with points of [7]. In particular, after a $200°$ rotation the mean cumulative error was of $23°$.

B. Real images and rotation

In this section we used the implementation of the algorithm with real omnidirectional images obtained with a

catadioptric system of a mobile robot. A ramp was used to have a rotation axis non-parallel to the mirror axis. A Gaussian filter was used to smooth the outdoor images. The objective is to recover the Euler angles of a pure rotation $R \in \mathcal{SO}(3)$ that gives us the relative orientation between *cameras*. The two omnidirectional images are the projection of these two cameras. Two particular real outdoor omnidirectional images that were used are shown in Figure 4.

Let bw be the band-limit of the discretization process, then the discretization errors of the Euler angles in the parameterization $Z(\gamma)Y(\beta)Z(\alpha)$ are given by $\Delta\alpha_{bw} = \Delta\gamma_{bw} = \frac{\pi}{2bw}$ and $\Delta\beta_{bw} = \frac{\pi}{4bw}$. In particular, for $bw = 16$, $\Delta\alpha_{16} = \Delta\gamma_{16} = 5.625°$, $\Delta\beta_{16} = 2.8125°$ and for $bw = 32$, $\Delta\alpha_{32} = \Delta\gamma_{32} = 2.8125°$, $\Delta\beta_{32} = 1.40625°$.

In the present work we are considering the general case where the rotation axis is not parallel to the z-axis. In the first case a ramp was used to get a rotation axis non-parallel to the mirror axis with $\alpha = \gamma = 0°$ and $\beta = 11.5°$, that is, a rotation with the y-axis only. Remember that x and y axes are on the image plane and the z-axis is orthogonal to it.

In the second case we used several Euler angles as shown in the Table I where five rotations were performed using the mobile robot. We can see from this Table that the recovered Euler angles with band-limits 16 and 32, have values of the errors $\Delta\alpha$, $\Delta\beta$ and $\Delta\gamma$ less than their discretization errors $\Delta\alpha_{bw}$, $\Delta\beta_{bw}$ and $\Delta\gamma_{bw}$, except for a pair of cases.

	I	II	III	IV	V
α	30°	50°	70°	80°	84°
β	11.35°	11.35°	11.35°	11.35°	11.35°
γ	10°	10°	15°	20°	20°

TABLE I

GROUND TRUTH ROTATION EULER ANGLES USED WITH REAL IMAGES.

The results using the algorithm of Radon with lines are basically the same as with points, but less points are needed, as we can see from Table I. In Table II we can see the total pair points of $S^2 \times S^2$ used with each of these algorithms to generate the results of Table I. Approximately a 23% less pair correspondences of lines were required with respect to points. Remembering that $3D$ points and $3D$ lines are points of S^2, then we are using 23% less points on S^2 that need to be processed with the tools of the harmonic analysis. This is an advantage with respect to the algorithm using $3D$ points, [7], [11].

	I	II	III	IV	V
RL	318	305	315	413	347
RP	394	377	423	546	469
$\Delta\%$	19%	19%	26%	24%	26%

TABLE II

PAIR CORRESPONDENCES USING RADON WITH LINES (RL) AND RADON WITH POINTS (RP) TO OBTAIN THE RESULTS OF TABLE I. THE PERCENTAGE CHANGE OF THE RATIO $\frac{|RL-RP|}{RP}$ SHOW US THAT WE NEED LESS PAIR CORRESPONDENCES USING LINES.

C. Conclusions

In this work the authors presented an application of the Radon transform to obtain the $3D$ rotation of a paracatadioptric system using lines without correspondences. The paracatadioptric model presented in [5] has been used to compute the back-projection of paracatadioptric lines onto the sphere. The algorithm shows an improvement of approximately 23% less information using lines than the algorithm with points [11], [7]. Real and synthetic images were used to test the algorithm. To obtain the Radon transform with lines we also require an analogous *epipolar constraint with points* and a *similarity function* for lines. Our algorithm takes advantage of the fact that lines are less noise sensitive than points. However, the algorithm of the Radon transform with lines will not be successful if it does not detect enough lines on the images. Thus, it will be necessary to find an algorithm for better lines detection. The authors believe that the use of a harmonic analysis based on Radon transform using lines is promising for omnidirectional image processing.

REFERENCES

[1] S. Baker and S. Nayar, "A theory of catadioptric image formation," *In Proc. Int. Conf. on Computer Vision*, vol. IV, pp. 35–42, 1998.

[2] T. Svoboda, T. Pajdla, and V. Hlavac, "Epipolar geometry for panoramic cameras," *In Proc. 5th European Conference on Computer Vision*, pp. 218–231, 1998.

[3] C. Geyer and K. Daniilidis, "A unifying theory for central panoramic systems and practical implications," *Proc. Eur. Conf. on Computer Vision*, pp. 445–461, 2000.

[4] E. Bayro-Corrochano and C. López-Franco, "Omnidirectional vision: Unified model using conformal geometry," *Proc. Eur. Conf. on Computer Vision*, pp. 318–343, 2004.

[5] C. López-Franco, N. Arana-Daniel, and E. Bayro-Corrochano, "Vision-based robot control with omnidirectional cameras and conformal geometric algebra," in *International Conference on Robotics and Automation*, 2010, pp. 343–349.

[6] C. Geyer, S. Sastry, and R. Bajcsy, "Euclid meets fourier: Applying harmonic anakysis to essential matrix estimation in omninidirectional cameras." *Workshop on Omnidirectional Vision*, 2004.

[7] K. Daniilidis, C. Geyer, A. Makadia, and S. Sastry, "Radon based structure from motion without correspondeces," in *Proceedings of CVPR 2005*, vol. 1, 2005, pp. 796–803.

[8] D. Hestenes, H. Li, and A. Rockwood, "New algebraic tools for classical geometry," in *Geometric Computing with Clifford Algebra*, G. Sommer, Ed., vol. 24. Berlin Heidelberg: Springer-Verlag, 2001, pp. 3–26.

[9] E. Bayro-Corrochano, Ed., *Robot perception and action using conformal geometric algebra*. Heidelberg: Springer-Verlag, 2005.

[10] H. Li and D. Hestenes, "Generalized homogeneous coordinates for computational geometry," in *Geometric Computing with Clifford Algebra*, G. Sommer, Ed., vol. 24. Berlin Heidelberg: Springer-Verlag, 2001, pp. 27–60.

[11] K. Daniilidis and A. Makadia, "Direct 3d-rotation estimation from spherical images via a generalized shift theorem," in *Proceedings of CVPR 2003*, vol. 2, 2003, pp. 217–224.

[12] D. Lowe, "Sift (scale invariant feature transform): Distinctive image features from scale-invariant keypoints." *International Journal of Computer Vision*, vol. 60, pp. 91–110, 2004.

[13] J. R. Driscoll and D. M. Healy, "Computing fourier transforms and convolutions on the 2-sphere." *Advances in Applied Mathematics*, vol. 15, pp. 202–250, 1994.

[14] P. Kostelec and D. Rockmore, "Ffts on the rotation group." *Working Paper Series, Santa Fe Institute*, 2003.